AGU PUBLICATIONS

Journal of Advances in Modeling Earth Systems

RESEARCH ARTICLE
10.1002/2016MS000627

Localizing the impact of satellite radiance observations using a global group ensemble filter

Lili Lei[1,2,3], Jeffrey L. Anderson[4], and Jeffrey S. Whitaker[3]

[1]Key Laboratory of Mesoscale Severe Weather, Ministry of Education, School of Atmospheric Sciences, Nanjing University, Nanjing, China, [2]Cooperative Institute for Research in Environmental Sciences, University of Colorado, Boulder, Colorado, USA, [3]Physical Sciences Division, NOAA/Earth System Research Laboratory, Boulder, Colorado, USA, [4]National Center for Atmospheric Research, Boulder, Colorado, USA

Key Points:
- Improve the assimilation of radiance observation
- Localizing the impact of radiance observation more effectively

Correspondence to:
L. Lei,
lililei@nju.edu.cn

Citation:
Lei, L., J. L. Anderson, and J. S. Whitaker (2016), Localizing the impact of satellite radiance observations using a global group ensemble filter, *J. Adv. Model. Earth Syst.*, *8*, 719–734, doi:10.1002/2016MS000627.

Received 8 JAN 2016
Accepted 19 APR 2016
Accepted article online 25 APR 2016
Published online 22 MAY 2016

Abstract Assimilation of satellite radiances has been proven to have positive impacts on the forecast skill, especially for regions with sparse conventional observations. Localization is an essential component to effectively assimilate satellite radiances in ensemble Kalman filters with affordable ensemble sizes. However, localizing the impact of radiance observations is not straightforward, since their location and separation from grid point model variables are not well defined. A global group filter (GGF) is applied here to provide a theoretical estimate of vertical localization functions for radiance observations being assimilated for global numerical weather prediction. As an extension of the hierarchical ensemble filter, the GGF uses groups of climatological ensembles to provide an estimated localization function that reduces the erroneous increments due to ensemble correlation sampling error. Results from an idealized simulation with known background error covariances show that the GGF localization function is superior to the optimal Gaspari and Cohn (GC) localization function. When the GGF is applied to the AMSU-A radiances, it can provide different localization functions for different channels, which indicates the complexity and large computational cost of tuning the localization scales for radiance observations. The GC, GGF, and fitted GGF (FGGF) localization functions are compared using experiments with the NCEP GFS and the NOAA operational EnKF. Verifications relative to the conventional observations, AMSU-A radiances, and the ECMWF analyses show that the GGF and FGGF have smaller errors than GC except in the tropics, and the advantages of the GGF and FGGF persist through 120 h forecast lead time.

1. Introduction

As a Monte Carlo approximation to the Kalman filter [*Kalman*, 1960], the ensemble Kalman filter (EnKF) [*Evensen*, 1994; *Burgers et al*., 1998] uses an ensemble of forecasts to estimate the background error covariances and then updates the state variables with observation information and assumed observation errors. The EnKF has been widely used for global [e.g., *Whitaker et al*., 2008; *Buehner et al*., 2010a, 2010b; *Houtekamer et al*., 2014] and regional [e.g., *Snyder and Zhang*, 2003; *Tong and Xue*, 2005; *Aksoy et al*., 2009] data assimilation systems, with assimilation of conventional observations, radar and satellite observations, and so on. For regions with sparse conventional observations, satellite radiances can have large positive impacts on the forecast skill [e.g., *Derber and Wu*, 1998; *Le Marshall et al*., 2006; *McNally et al*., 2006; *McCarty et al*., 2009; *Collard and McNally*, 2009], since the widely available satellite radiances provide important information about temperature, wind, and moisture.

When the EnKF is applied in high-dimensional geophysical applications, affordable ensemble sizes are often order of 100, much smaller than the number of state variables. The EnKF is subject to sampling error that can lead to degraded analyses and filter divergence. To combat sampling error, strategies like covariance inflation [e.g., *Anderson* and *Anderson*, 1999; *Whitaker et al*., 2008; *Anderson*, 2009] and localization [e.g., *Houtekamer and Mitchell*, 2001; *Hamill et al*., 2001] have been developed. Covariance localization limits the impact of observations on remote state variables to reduce detrimental effects from spurious correlations. However, covariance localization for satellite radiances is not straightforward because the concepts of location and vertical separation for satellite radiances (nonlocal observations) are not well defined. *Campbell et al*. [2010] suggested that localizing the impact of radiance observations in model space was more accurate than localizing in observation space. But *Lei and Whitaker* [2015] documented situations where the opposite is true.

To apply localization for radiance observations, *Houtekamer et al*. [2005] and *Houtekamer and Mitchell* [2005] treated the Advanced Microwave Sounding Unit-A (AMSU-A) radiance observations as local observations whose vertical locations were given by the level with maximum weighting function and applied a *Gaspari and Cohn* [1999] (GC) localization function. To better extract information from the radiances, *Miyoshi and Sato* [2007] and *Miyoshi et al*. [2010] used the normalized sensitivity function as a vertical localization function for the radiances from different satellite platforms and found positive impacts. Instead of assigning vertical locations for radiance observations, the radiance observations that are strongly correlated to a model grid point could be used to update the model state [*Fertig et al*., 2007]. *Otkin* [2012] studied the impact of horizontal localization scale on the assimilation of infrared brightness temperature observations without vertical localization applied since the brightness temperature is sensitive to broad layers of the atmosphere. Given this diversity of localization approaches, theoretical studies for vertical localization of radiance observations are needed.

Among the candidate methods that can provide theoretical estimates for the localization functions of radiances, one is the hierarchical ensemble filter introduced by *Anderson* [2007], and another is the empirical localization function proposed by *Anderson and Lei* [2013]. The hierarchical filter utilizes a group of ensembles that run simultaneously and obtains a sample of the regression coefficient between an observation and a state variable. A localization value is then computed based on the sample of the regression coefficient aiming to minimize the sampling error. *Anderson* [2007, Figure 12] presented the estimated localization function for an integral observation (average of 15-point observations). The estimated localization function is flat and has value less than 1 around the observation "location" and gradually decreases to 0 with increasing separation. Unlike the hierarchical filter that uses a group of ensembles simultaneously, the empirical localization often uses the output of an ensemble observing system simulation experiment (OSSE) and assumes the true state is known. For a subset of pairs of observations and state variables, a localization value is computed by minimizing the root-mean-square (RMS) difference between the true value and the posterior ensemble mean. The estimated empirical localization function for an integral observation (average of 17-point observations) shown in *Anderson and Lei* [2013, Figure 9] is very similar to that of *Anderson* [2007, Figure 12].

Lei and Anderson [2014a] compared the empirical localization function and an extension of the hierarchical ensemble filter called the global group filter (GGF). The GGF uses a group of offline ensembles to estimate the sampling error, and it computes a localization value that minimizes the sampling errors for all pairs of observations and state variables in a subset. Although in some situations the GGF may underestimate the localization value compared to the empirical localization function, it does not require knowledge of the true state (unknown for real applications) and does not explicitly need the separations between observations and state variables. Thus, a GGF that is based on climatological ensemble perturbations (details in section 2) is used to estimate the vertical localization for radiance observations in this study. The estimated vertical localization function from the GGF can provide guidance for localizing radiance observations, since it is designed to minimize the sampling error of an ensemble assimilation system.

This article is structured as follows. In section 2, the methodology of a GGF based on climatological perturbations is described. To demonstrate the efficacy of this approach for radiance observations, an idealized simulation is conducted in section 3 for two kinds of background error covariances. Section 4 conducts experiments in the NCEP Global Forecast System (GFS). The estimated vertical localization functions from the GGF for the AMSU-A radiances are investigated, and results with the GGF applied in subsequent assimilation experiments are discussed. Section 5 discusses and summarizes the results.

2. Methodology

A procedure that is similar to the hierarchical ensemble filter proposed by *Anderson* [2007] and the GGF used by *Lei and Anderson* [2014a] is used to construct vertical localization functions for satellite radiances. From an existing ensemble simulation, climatological perturbations of the ensemble prior estimates of the observations and state variables are collected. Subsets of these perturbations are then randomly selected and used to compute the sample correlations between the observations and state variables, and the same sample correlations can be computed between observations and observations. By minimizing the sampling

error of the estimated correlations, a confidence factor, i.e., the localization value, is computed following *Lei and Anderson* [2014a].

Given an ensemble simulation experiment, define $\mathbf{Y}$ as the set of all ensemble prior estimates of the observations that were assimilated in the simulation. Let $y_{l,n}$ be an element of $\mathbf{Y}$, $l \in \{1,\ldots, L\}$ and $n \in \{1,\ldots, N\}$, where L is the total number of observations and N is the ensemble size. Define $\Delta\mathbf{Y}$ as the set of all perturbations of the ensemble prior estimates of the observations. An element $\Delta y_{l,n}$ of $\Delta\mathbf{Y}$ is given by $\Delta y_{l,n}=y_{l,n}-\overline{y_l}$, where $\overline{y_l}$ denotes the ensemble mean of the lth observation.

Define $\mathbf{X}$ as the set of state variables that are interpolated to the horizontal locations of observations. An element of $\mathbf{X}$, $x^k_{l,n}$, $k \in \{1,\ldots, K\}$, where K is the number of model vertical levels, has the same horizontal location as y_l. Define $\Delta\mathbf{X}$ as the set of all perturbations of ensemble state variables in $\mathbf{X}$. An element of $\Delta\mathbf{X}$ is $\Delta x^k_{l,n}=x^k_{l,n}-\overline{x^k_l}$, where the overbar denotes the ensemble mean.

Since the vertical location of radiance observations and the vertical separations between radiances and state variables are not well defined, the localization function can be defined as a function of vertical coordinate instead of vertical separation. Here pressure is used as the vertical coordinate. Define $\Delta\mathbf{X}_s$ as a subset of $\Delta\mathbf{X}$, which contains perturbations of state variables whose pressure locations are between $(s-1)^*\ \Delta p$ and $s^*\Delta p$, where Δp is pressure interval. The set of all pairs $(\Delta y, \Delta x)$, where $\Delta y \in \Delta\mathbf{Y}$, and $\Delta x \in \Delta\mathbf{X}_s$ comprise the sth subset and is used to compute the localization value for the subset. Using N random samples from subset s, an estimate of the climatological correlation between y and x can be computed by $r=\dfrac{\sum_{i=1}^{N}\Delta x_i\Delta y_i}{\sqrt{\sum_{i=1}^{N}\Delta x_i^2\sum_{i=1}^{N}\Delta y_i^2}}$. *Anderson* [2007] used a group of ensemble filters (with a group size G) to obtain an estimate of the distribution of the regression coefficient between one observation and a state variable. *Lei and Anderson* [2014a] used an offline ensemble simulation and collected regression coefficients for all samples in a subset (with a sample size M). Here repeating the process of computing the climatological correlation $M\times G$ times, a set of estimated climatological sample correlations is obtained, which is denoted by r^g_m, $g \in \{1,\ldots, G\}$ and $m \in \{1,\ldots, M\}$.

The localization value α is defined to minimize the sampling error of the estimated climatological sample correlations. Here sample correlation is used instead of sample regression coefficient that is used by *Anderson* [2007] and *Lei and Anderson* [2014a], because $\Delta\mathbf{X}$ and $\Delta\mathbf{Y}$ contain all perturbations from one ensemble simulation and the estimated sample regression coefficients are not bounded. *Anderson* [2012] demonstrated that sampling error in the estimated regression coefficients mainly comes from that in the estimated correlations for all except very small ensemble sizes. Thus, a localization value based on sample correlations is expected to be similar to that based on sample regression coefficients. Following *Lei and Anderson* [2014a, equation (2)], α can be computed by

$$\alpha=\frac{\sum_{m=1}^{M}\left(\sum_{g=1}^{G}r^g_m\right)^2/\sum_{m=1}^{M}\sum_{g=1}^{G}\left(r^g_m\right)^2-1}{G-1}, \tag{1}$$

which minimizes the RMS difference between the estimated correlations for all the pairs in the subset. Following this procedure to compute a localization value α for each subset s, a localization that is a function of the state variable pressure can be obtained.

3. Idealized Simulation

The GGF is first examined in an idealized simulation where the true error covariance is known. The idealized 1-D model used by *Lei and Whitaker* [2015] to compare the differences between model space and observation-space localization for radiance observations is adopted here. The true error covariance is either Gaussian or the second derivative of a Gaussian [*Lei and Whitaker*, 2015]. Unlike the Gaussian error covariance, the second derivative of a Gaussian has some negative correlations.

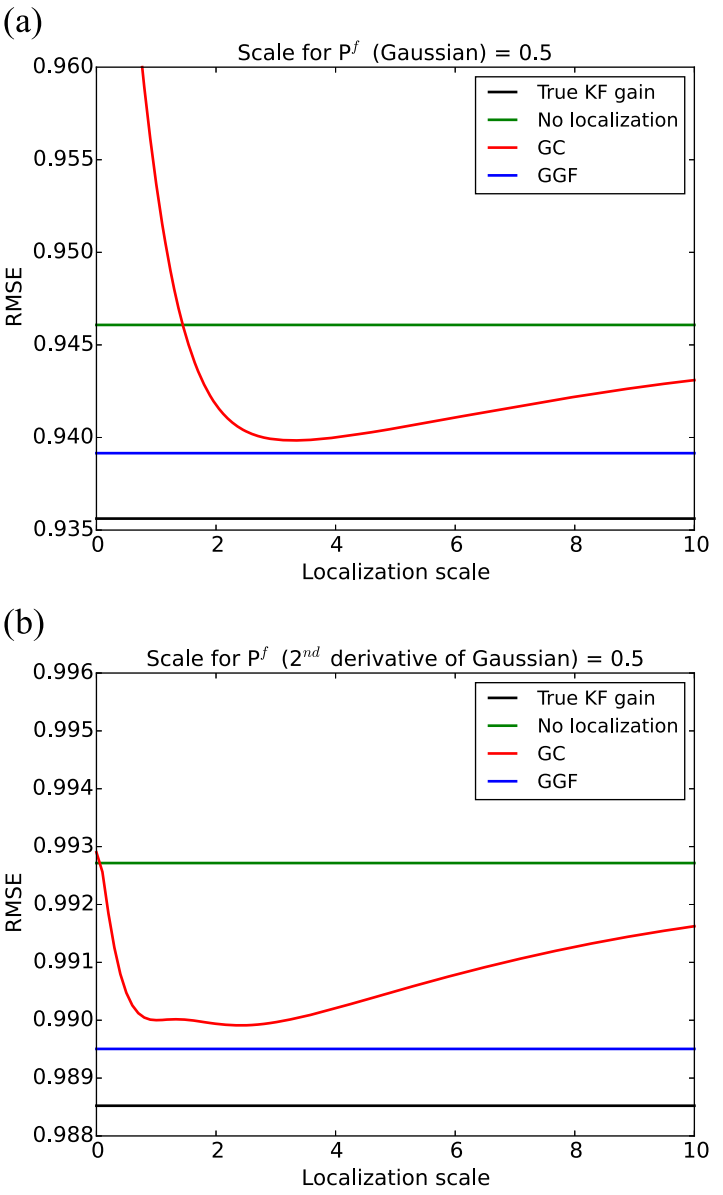

Figure 1. Average analysis RMSE with 40 members and varying localization scales when the true covariance is (a) Gaussian and (b) the second derivative of a Gaussian. The green line presents the RMSE using the estimated Kalman gain without localization, and the blue line displays the RMSE using the estimated Kalman gain with GGF localization function, while the black line denotes the RMSE using the true Kalman gain.

The 1-D model has 101 equally distributed vertical levels of $-ln(p/p_s)$ between p_s and 10 hPa, where p_s is 1000 hPa. The true state values are assumed to be 0 for all levels, and the *e*-folding scale for the true error covariances is 0.5. The sample error covariance is obtained by randomly sampling the true error covariance with 40 ensemble members. The forward operator **H** is a vertical average with Gaussian kernel with an *e*-folding scale 1.0. A single observation that has **H** peaking at level 25 with pressure 331 hPa is generated by adding random draws from a normal distribution $N(0, 0.1)$ to the true observation value.

The GC localization function is used as a reference. Its localization scale at which observation impact decreases to 0 varies from 0 to 10.0. There are 10,000 trials for each localization scale. The correlations from the 10,000 trials are divided into four groups ($G = 4$ and $M = 10{,}000/4$) to construct the GGF localization function using equation (1) for each vertical level. The GGF localization function is then applied for 10,000 trials. For each localization scale, the sample Kalman gain is computed, and an analysis is produced. The root-mean-square error (RMSE) of the analysis relative to the true state is calculated and averaged over the 10,000 trials.

Figure 1 shows the RMSE with varying localization scales when the true error covariances are either Gaussian or the second derivative of a Gaussian. For the two kinds of true error covariances, there is an optimal GC localization scale that gives the smallest RMSE. The GGF localization function produces smaller RMSE than the optimal GC localization functions in both cases, consistent with *Anderson and Lei* [2013] and *Anderson* [2016].

Figure 2 displays the GGF and optimal GC localization functions for the two kinds of true error covariances. When the true error covariance is Gaussian, the mean sample correlation is less than one at the assigned observation location (level 25), and monotonically decreases with increasing separations. Consistent with the mean sample correlation, the GGF has value slightly less than one at the assigned observation location and gradually decreases to 0 with separation. The optimal GC localization function has value 1.0 at the assigned observation location, and has values smaller than the GGF when separations are smaller than 1.0 but broader tails than the GGF.

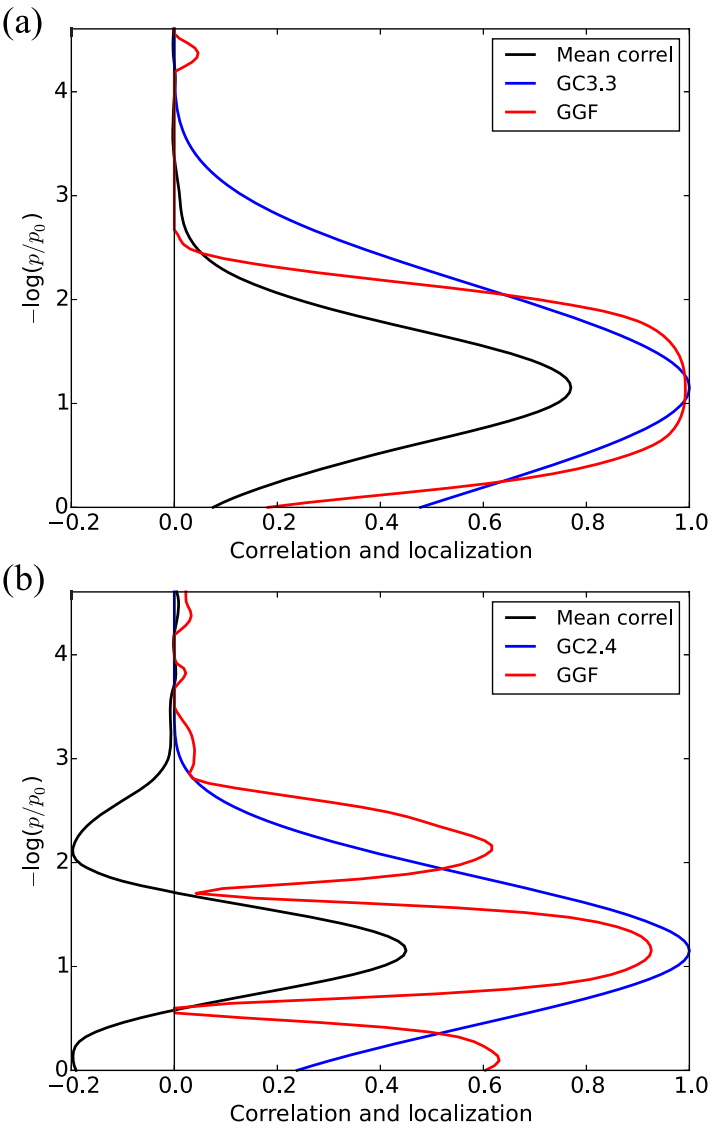

Figure 2. Mean sample correlations (black), optimal GC localization function (blue), and the GGF localization function (red) for (a) Gaussian and (b) the second derivative of a Gaussian true covariances.

When the true error covariance is the second derivative of a Gaussian, the mean sample correlation is less than one around the assigned observation location, and it contains negative correlations by design. The GGF is consistent with the absolute value of the mean sample correlations. The GGF has values less than one at the assigned observation location, and it decreases with separation with a value of 0 when the mean sample correlation is approximately 0. When the sample correlations become negative, the GGF increases and has a maximal value of 0.6 when the mean sample correlation is minimum. The optimal GC localization function has narrower localization scale than the GGF, but it has larger values than the GGF around the assigned observation locations.

Figure 3 shows the maximum RMSE reduction (minimum analysis RMSE that can be obtained with optimal localization parameters divided by the forecast RMSE) from GC and GGF localization functions with varying ensemble size. For all ensemble sizes, the differences of the maximum RMSE reduction between GC and GGF localizations are statistically significant at the 95% confidence level using a paired sample *t* test. With varying ensemble size, previous results (Figure 1) hold: GGF localization produces larger error reduction than the optimal GC localization for the two kinds of true error covariances. The differences between GC and GGF localizations generally become smaller with increasing ensemble size.

This idealized simulation demonstrates that the GGF can provide appropriate localization functions for nonlocal observations, especially when there are negative error covariances, and these estimated localization functions can outperform the best GC localization function. The next step is to construct the GGF localization function for real radiance observations and apply the GGF in subsequent assimilation experiments.

4. NCEP GFS Simulation

The GGF is used to construct vertical localization functions for the AMSU-A radiances, since the assimilation of the AMSU-A radiances has significant positive impact on global forecast skills [e.g., *Zapotocny et al.*, 2008; *Ota et al.*, 2013]. Experiments that assimilate only AMSU-A radiances with different localization functions will be described in section 4.1. The vertical GGFs that are constructed from the output of the experiment

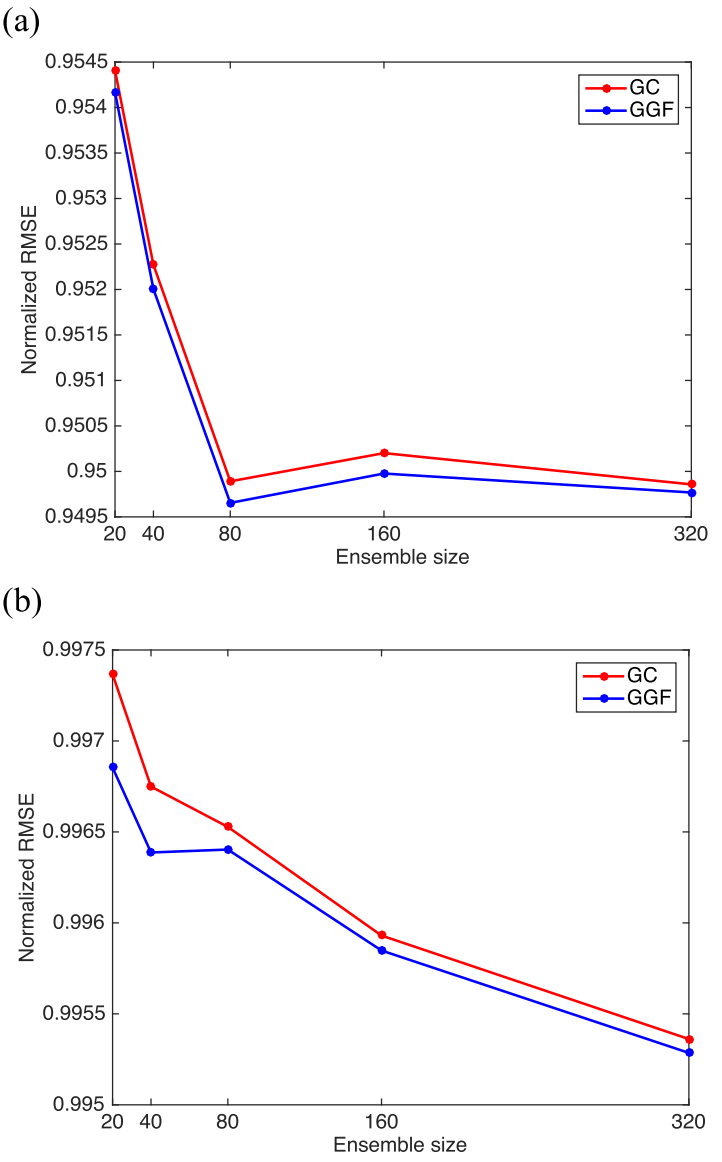

Figure 3. The maximum analysis RMSE reduction (minimum analysis RMSE divided by the forecast RMSE) from GC and GGF localization functions with varying ensemble size for (a) Gaussian and (b) the second derivative of a Gaussian true covariances.

using the GC localization function and the fitted GGF (FGGF) that uses GC function to fit the GGFs will be presented in section 4.2. Sections 4.3 and 4.4 will discuss the results using GC, GGF, and FGGF localization functions.

4.1. Experimental Design

Three ensemble assimilation experiments (EnKF-GC, EnKF-GGF, and EnKF-FGGF) with 80 ensemble members are conducted using the NCEP Global Forecast System (GFS) model with a resolution T254L64 and model top 27 Pa. They extend from 00UTC 1 April 2014 to 00UTC 15 April 2014. AMSU-A radiance observations (http://www.emc.ncep.noaa.gov/mmb/data_processing/prepbufr.doc/table_18.htm) that are used in the NCEP Global Data Assimilation System (GDAS) are assimilated every 6 h. Channels 1–3 and 15 are sensitive to surface conditions and channel 14 is sensitive to conditions above the model top, thus these channels are not assimilated. The grid point statistical interpolation (GSI) [*Wu et al.*, 2002; *Kleist et al.*, 2009] is used to compute the observation forward operator $\mathbf{H}$ and save the values of $\mathbf{Hx}^b$ for the ensemble mean and each ensemble member separately. The observation error variance $\mathbf{R}$ uses the same values as in the NCEP GDAS.

For all experiments, horizontal localization uses the GC localization function that tapers the observation impact to 0 at 1250 km. This horizontal localization scale is empirically chosen without tuning, but we expect general results will be hold with a different horizontal localization scale, since radiance observations are integral observations in the vertical. For the vertical localization, experiment EnKF-GC uses the GC localization function with length scale of 1.0 (unit: *ln*(hPa)). Vertical GGFs for each channel of the AMSU-A radiance observations and state variable temperature are computed using the output of EnKF-GC. Experiment EnKF-GGF (EnKF-FGGF) uses the vertical GGFs (FGGFs) for both state update and observation update (details will be discussed in section 4.2). Although *Hamurd et al.* [2015] showed different correlations for the AMSU-A radiances with temperature and zonal wind, the vertical GGFs between the AMSU-A radiances and temperature are only used here to keep the simplicity, and the application of the vertical GGFs between the radiance observations and each state variable and observation type will be explored in a future study.

The ensemble square root filter (EnSRF) [*Whitaker and Hamill*, 2002; *Whitaker et al.*, 2008] in the NOAA operational EnKF (http://www.dtcenter.org/com-GSI/users/docs/enkf_users_guide/EnKF_UserGuide_v1.

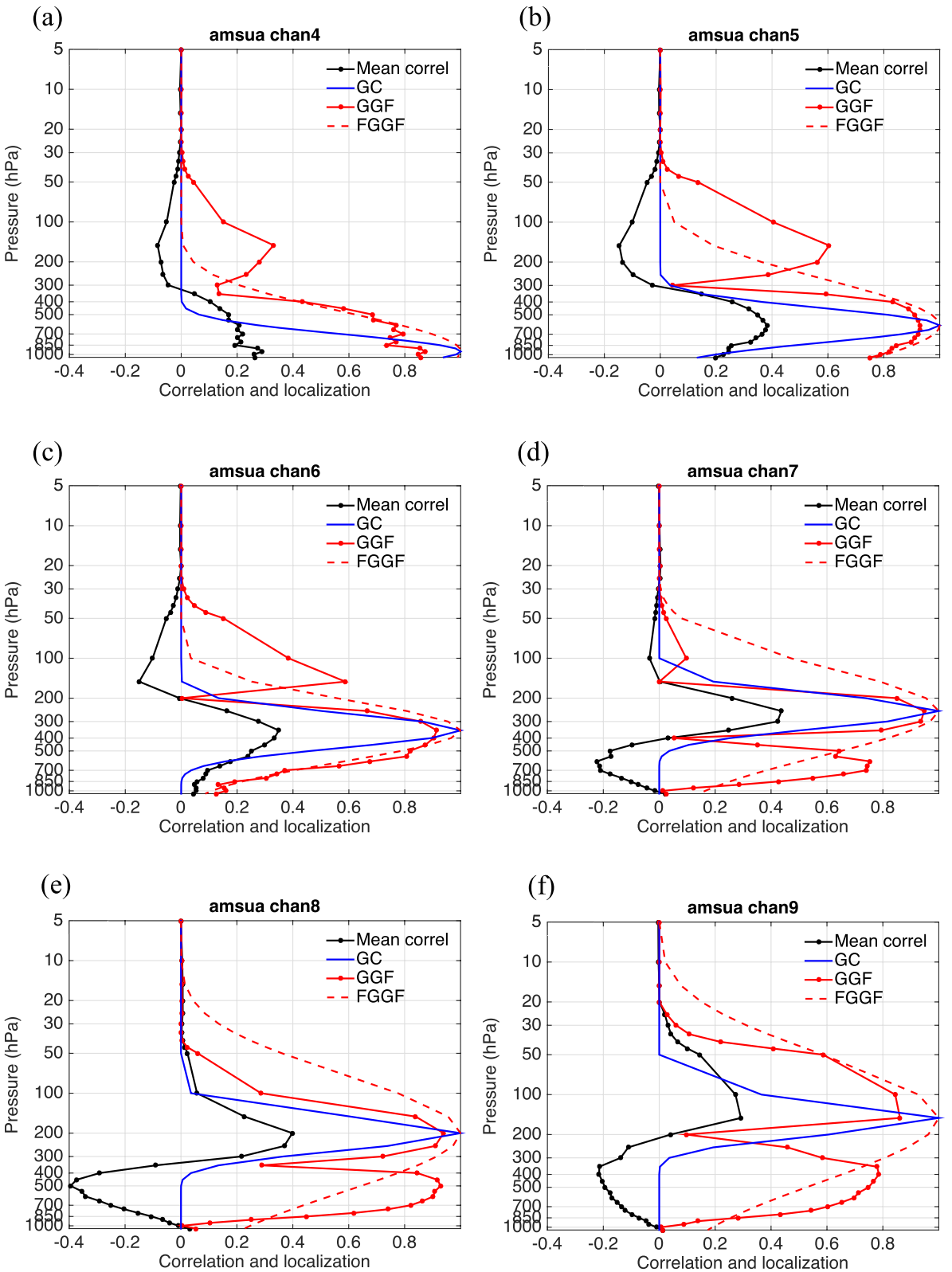

Figure 4. Mean sample correlations (black), reference GC localization function (blue), GGF localization function (red-solid), and fitted GGF localization function (FGGF; red dashed) for the wind channels 4–13 of the AMSU-A radiances.

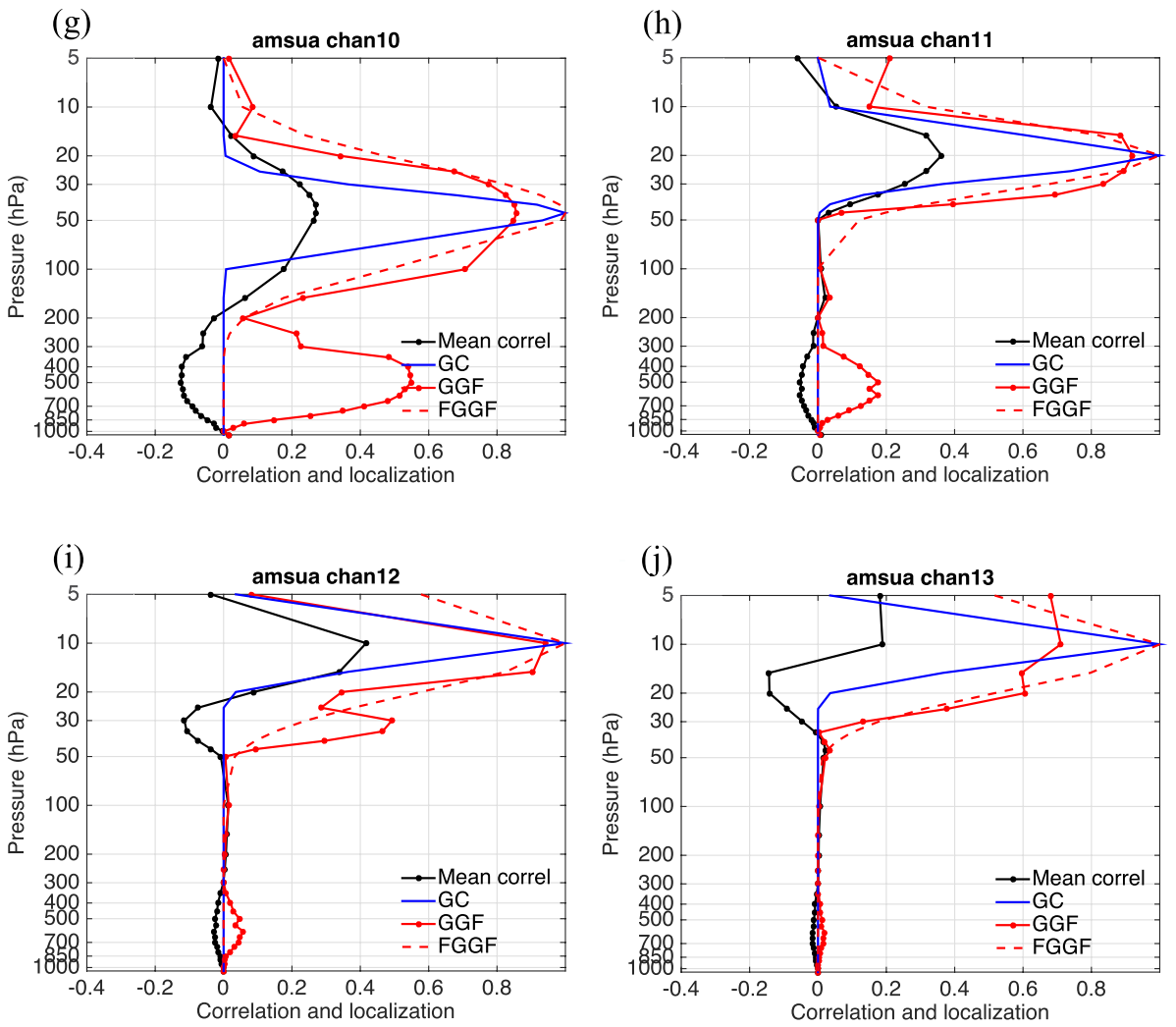

Figure 4. (continued)

0Beta.pdf) is used to assimilate the observations. To maintain appropriate ensemble spread and avoid filter divergence, multiplicative covariance inflation that relaxes posterior ensemble spread back to prior ensemble spread (relaxation-to-prior spread) [*Whitaker and Hamill*, 2012] is used with relaxation coefficient 0.85; no additive inflation is applied. During model integration, stochastic physics [*Palmer et al*., 2009] are used to represent the model uncertainty.

4.2. Estimated Vertical Localization Function

The 6 h output between 00UTC 5 April 2014 and 00UTC 7 April 2014 from experiment EnKF-GC is used to compute the vertical GGF localization function for the AMSU-A radiances. The observation priors of the AMSU-A radiances are computed by the Community Radiative Transfer Model (CRTM) [*Weng*, 2007; *Han et al*., 2007] for each ensemble member. The ensemble of the observation priors constitutes the set **Y**. The prior ensembles of temperature profiles at the observation locations and times are interpolated from the prior ensemble of the EnKF-GC experiment, which constitutes the set **X**. Here vertical separation Δp is set to 5 hPa when pressure is smaller than 50 hPa and 50 hPa otherwise. Given the set **Y** and **X**, the GGF localization function for each channel of the AMSU-A radiances in the vertical is computed following the procedures described in section 2 with $G = 16$ and $M = 100{,}000$.

The mean sample correlations and GGF localization functions for channels 4–13 are shown in Figure 4. The correlation between the AMSU-A radiance observations from channel 4 and temperature is approximately

Table 1. The Localization Length Scales of the FGGFs for Each Channel of the AMSU-A Radiance Observations

Channel	4	5	6	7	8	9	10	11	12	13
FGGF length scale (unit: *ln*(hPa))	2.3	2.7	1.8	2.6	3.4	3.7	2.3	1.6	2.3	2.1

0.3 at 950 hPa, and it decreases with height (Figure 4a). It is negative between 300 and 30 hPa, and approaches 0 above 30 hPa. The estimated localization function has similar shape to the absolute value of the correlation, which is consistent with the idealized simulation in section 3. The GGF has value of approximately 0.9 at 950 hPa and initially decreases with height. However, it has a local maximum value corresponding to the local minimum correlation. As a reference, a GC localization function with a length scale of 1.0 (unit: *ln*(hPa)) is computed for which the vertical observation "location" is assigned as the pressure level of the maximum mean sample correlation. Comparing to the GC localization function, the GGF is less than 1.0 around the vertical observation "location," and it has a larger length scale and broader tail.

From channel 4–13, the level with the maximum positive correlation moves upward. Away from the level with the maximum positive correlation, the correlation decreases, and it can become negative. There are particularly strong negative correlations for channels 7–9. The estimated localization functions have similar shape to the absolute values of the correlation. When close to the vertical observation "location," the localization value has a maximum slightly less than 1.0. It decreases away from the observation "location," and reduces to 0 when the correlation becomes 0. However, the estimated localization values become significantly positive when there are prominent negative correlations leading to an additional local maximum of the localization function. Compared to the GC localization functions, the GGFs have value less than 1.0 around the vertical observation "location", and they have larger length scales. More importantly, the GGF localization function is often bimodal, clearly non-Gaussian.

To produce a smooth localization function, the GC function is used to fit the GGF. The GC function that has the smallest RMS difference comparing to the GGF is denoted as FGGF and displayed by the red-dashed line in Figure 4. The localization scales of the FGGFs for each channel of the AMSU-A radiances are shown in Table 1. For each channel, the FGGF has larger length scale than the reference GC function, which is consistent with the GGF. The FGGF has larger localization values than the GGF around the observation "location" and broader length scale than the GGF, because it tends to include the local maxima of GGF that are resulted from negative correlations.

4.3. Verification of the Estimated Vertical Localization Function

The GGF localization functions discussed in section 4.2 have different shapes from the commonly used GC localization function, and they vary significantly among channels. Without prior information of localization scale, tuning GC functions for each channel would be difficult and costly. The FGGFs suggest broader localization length scales than 1.0 (unit: *ln*(hPa)) used by EnKF-GC, thus an additional experiment EnKF-GC2.4 is conducted with a GC localization length scale 2.4 (unit: *ln*(hPa)) that is similar to the localization length scale used in *Hamurd et al*. [2015]. In this section, the GGF and FGGF localization functions are applied in additional assimilation experiments (EnKF-GGF and EnKF-FGGF), and then compared to experiments EnKF-GC and EnKF-GC2.4. The first 4 days of assimilation are discarded to avoid transient effects and the remaining data between 00 UTC 5 April 2014 and 00 UTC 15 April 2014 are evaluated.

The observation-space diagnostics use the 6 h prior. The average error profiles of wind speed verified relative to the conventional observations are shown in Figure 5. The errors are averaged globally (GL), in the Northern Hemisphere (NH; 20°N–90°N), the Tropics (TR; 20°S–20°N), and the Southern Hemisphere (SH; 90°S–20°S), respectively. EnKF-GGF produces smaller errors than EnKF-GC and EnKF-GC2.4 in the NH and SH, and also GL, but it has slightly larger errors than EnKF-GC and EnKF-GC2.4 in the TR. EnKF-FGGF produces smaller errors than EnKF-GC and EnKF-GC2.4 in the NH, SH, and GL, and it produces similar errors to EnKF-GC and EnKF-GC2.4 in the TR. Comparing to EnKF-GGF, EnKF-FGGF produces slightly smaller errors in the NH and SH, and smaller errors in the TR. Similar results are obtained for temperature but the differences among the experiments are smaller (not shown).

Figure 6 displays the verification of the 6 h priors relative to the AMSU-A radiance observations. All three experiments have similar errors for channel 13 and the errors of channel 13 are much larger than for the other channels, thus the errors of channel 13 are not shown in order to clearly show the differences among

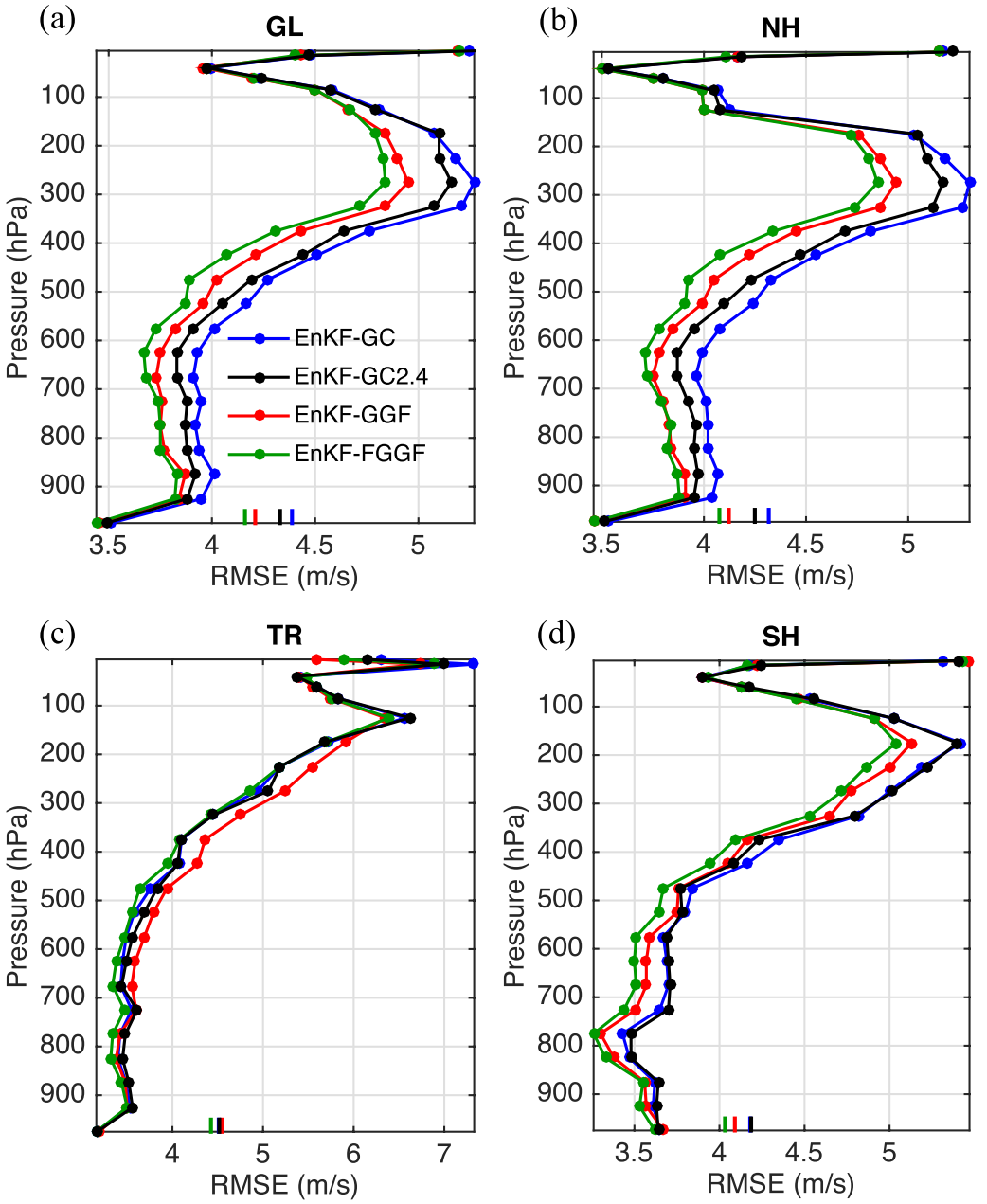

Figure 5. Average error profiles of wind speed for (a) the globe, (b) the Northern Hemisphere (NH), (c) the tropics (TR), and (d) the Southern Hemisphere (SH), which are computed from the 6 h initial forecast (prior) verified relative to the conventional observations. The bars on bottom denote the mean value of the error.

the experiments for the other channels. In the NH and SH, EnKF-GGF and EnKF-FGGF have similar errors, and both have smaller errors than EnKF-GC and EnKF-GC2.4, especially for channels 6–9. In the TR, EnKF-FGGF produces very slightly smaller errors than EnKF-GGF, EnKF-GC, and EnKF-GC2.4.

The 6 h priors are also verified in model space by comparing to the ECMWF operational analyses. The forecasts from the experiments are converted to resolution 1° with 37 vertical levels that are distributed from 1000 to 100 hPa, and the 1° forecasts are then evaluated relative to the ECMWF 1° analyses. For each experiment, the absolute error is averaged over longitude and the verification period. The differences of the averaged absolute error between EnKF-GGF and EnKF-GC for temperature and wind are shown in Figure 7. Figure 8 presents the differences between EnKF-FGGF and EnKF-GC. Cold (warm) color denotes that EnKF-GGF or EnKF-FGGF has smaller (larger) absolute error relative to the ECMWF analyses than EnKF-GC.

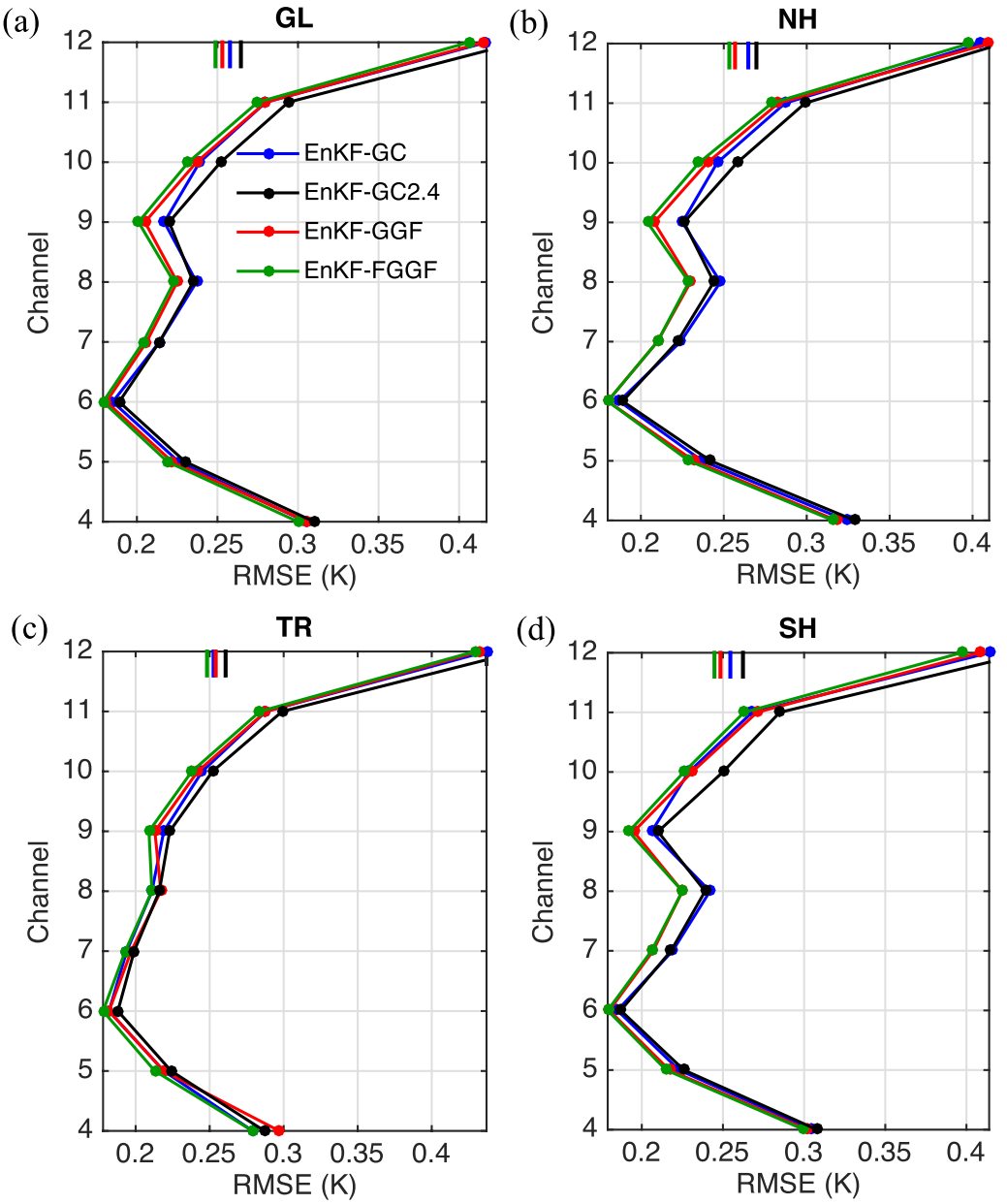

Figure 6. Average error profiles of AMSU-A radiances for (a) the globe, (b) NH, (c) TR, and (d) SH, which are computed from the 6 h initial forecast (prior) verified relative to the AMSU-A radiance observations. The bars on top denote the mean value of the error.

As shown by Figure 7a, EnKF-GGF has smaller temperature error than EnKF-GC in the NH and SH extending from the surface to 150 hPa. It has slightly larger temperature error than EnKF-GC in the TR. Similar results are obtained for wind speed (Figure 7b), while EnKF-GGF has smaller wind error than EnKF-GC in the midlatitudes, especially between 700 and 200 hPa. Similar error patterns are obtained between EnKF-FGGF and EnKF-GC (Figure 8), except that EnKF-FGGF has similar error of temperature and wind speed to EnKF-GC in the TR. Comparing Figure 8 with Figure 7, EnKF-FGGF produces similar errors relative to the ECWMF analyses to EnKF-GGF, except that EnKF-FGGF has smaller error than EnKF-GGF in the TR, which is consistent with the observation-space diagnostics.

To examine whether the differences among the experiments persist for longer forecasts, 5 day forecasts are initialized from each analysis during the verification period for the three experiments. Forecasts are verified against the ECMWF analyses for 1–5 day leads, and the absolute error of each experiment is averaged globally and over the verification period. Figure 9 presents the differences of the averaged absolute error

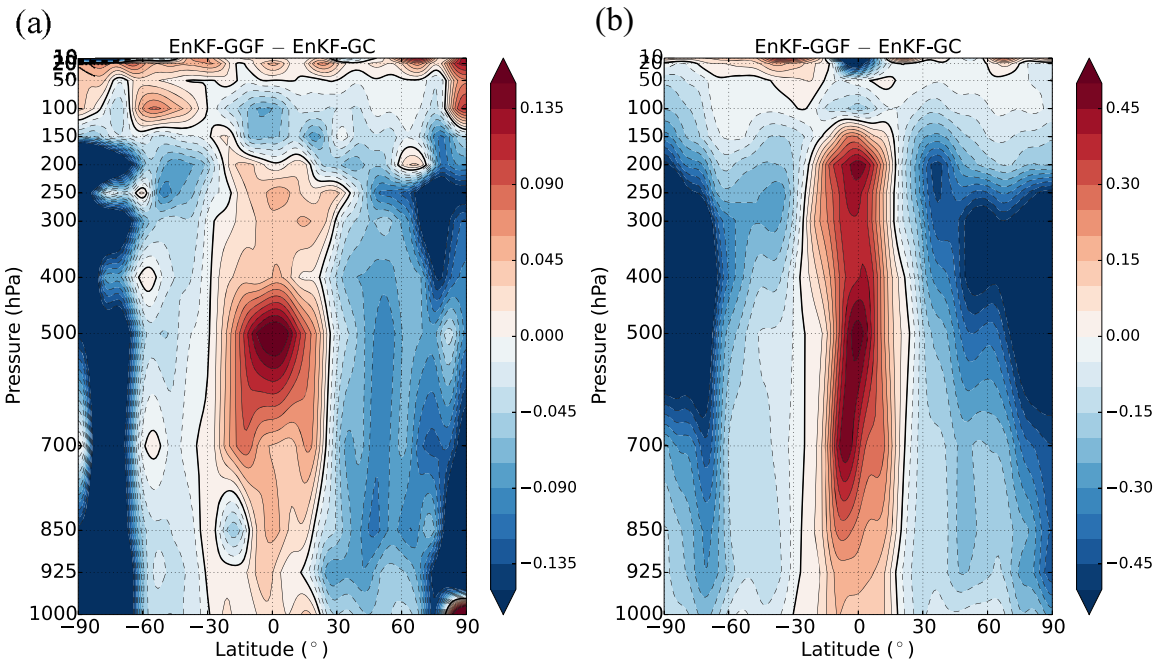

Figure 7. The difference of absolute error of (a) temperature and (b) wind speed between experiments EnKF-GGF and EnKF-GC. The error is computed by verifying against the ECMWF analysis and averaged over longitude and verification period. Cold (warm) color means EnKF-GGF has smaller (larger) error relative to the ECMWF analyses than EnKF-GC.

between experiments EnKF-GGF and EnKF-GC at different forecast lead times. Negative values indicate that EnKF-GGF has smaller error relative to the ECMWF analyses than EnKF-GC. For temperature, the negative values extend from the surface to 50 hPa for all lead times. Similar results are obtained for wind speed with the largest error differences around 250 hPa. The differences of the averaged absolute error between experiments EnKF-FGGF and EnKF-GC are displayed in Figure 10. EnKF-FGGF produces smaller errors of

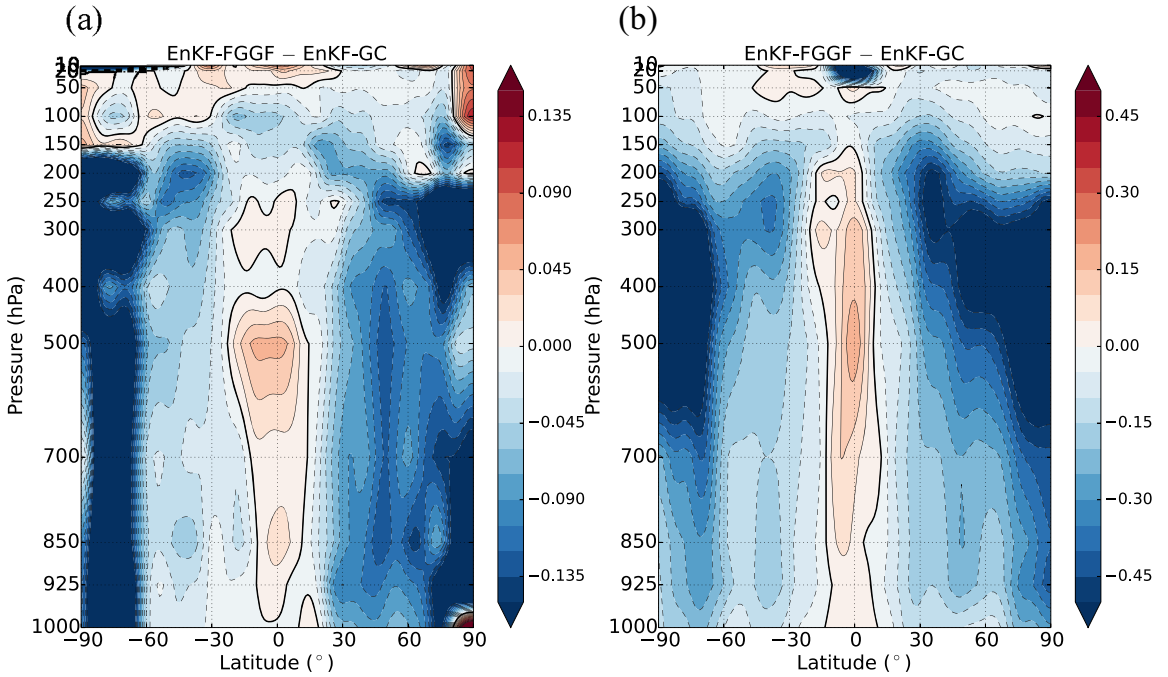

Figure 8. Same as Figure 7, but between experiments EnKF-FGGF and EnKF-GC.

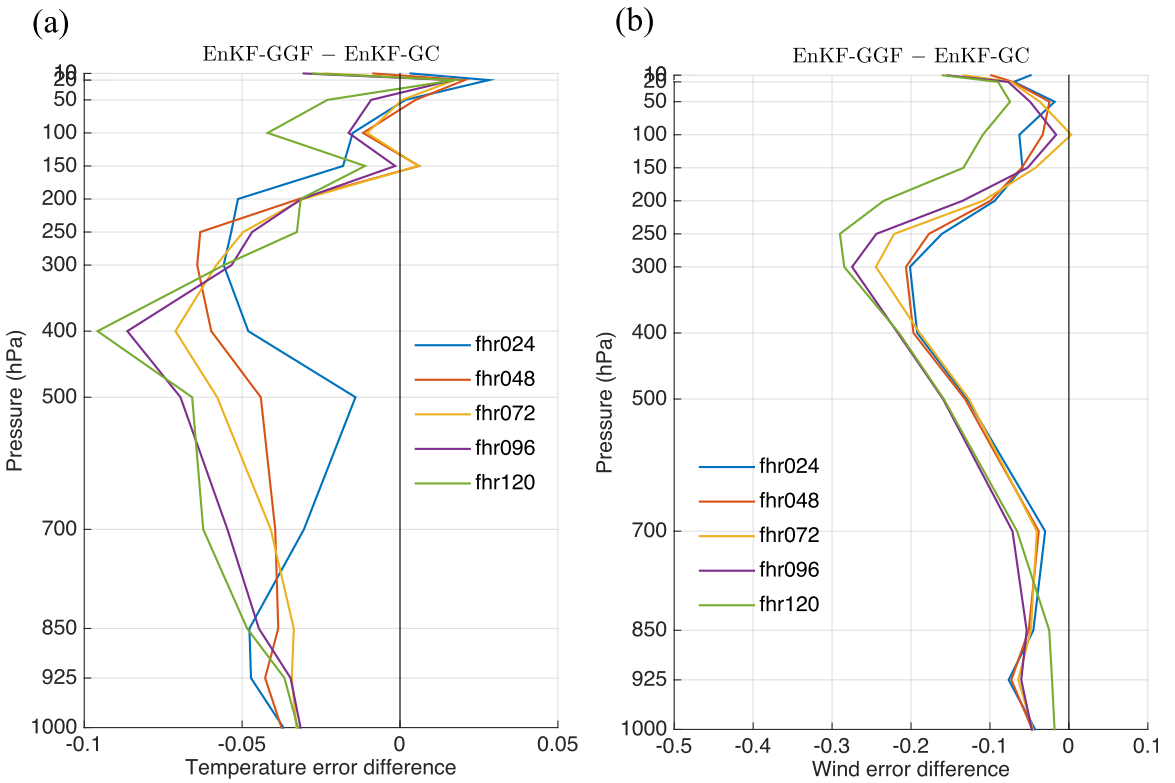

Figure 9. Profiles of difference of absolute error for (a) temperature and (b) wind speed between experiments EnKF-GGF and EnKF-GC at different forecast lead times. The error is computed by verifying against the ECMWF analysis and averaged globally and over the verification period. Negative values indicate that EnKF-GGF has smaller error relative to the ECMWF analyses than EnKF-GC.

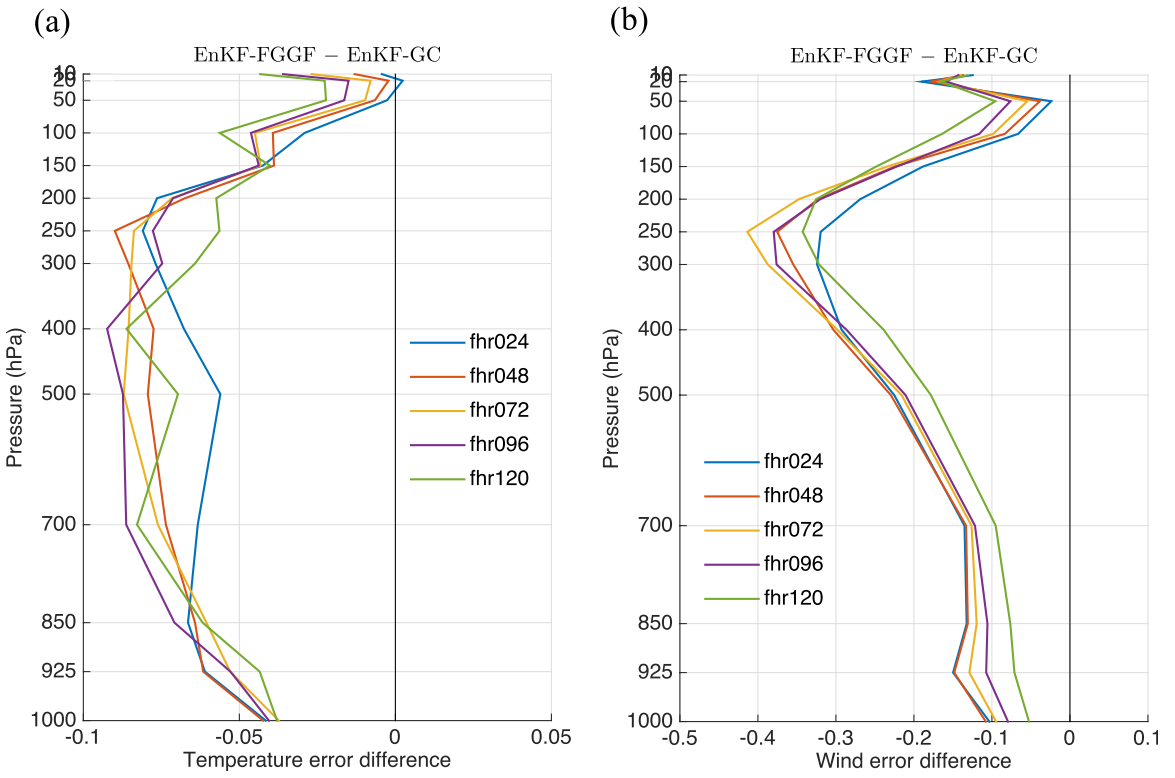

Figure 10. Same as Figure 9, but between experiments EnKF-FGGF and EnKF-GC.

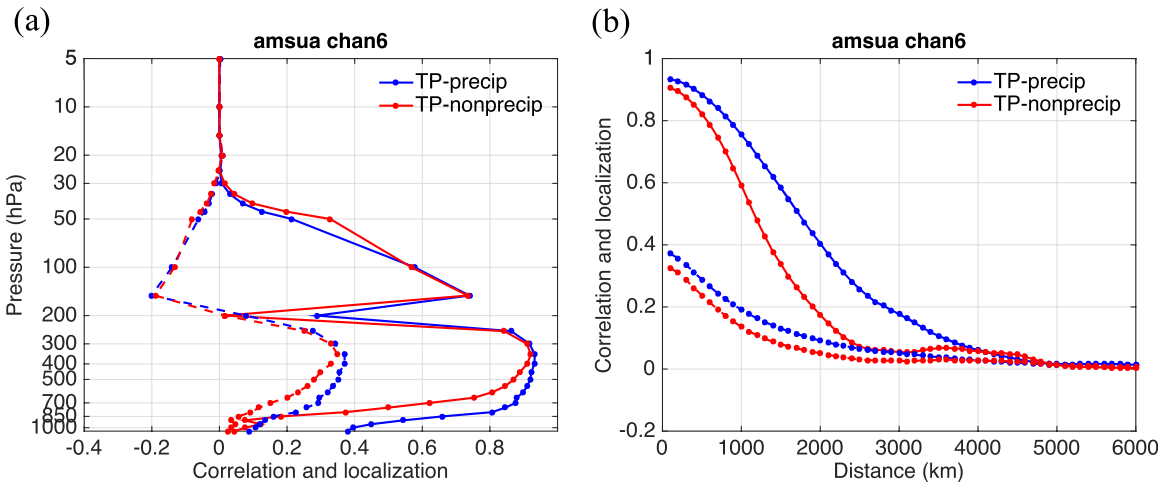

Figure 11. GGF localization function (solid) and mean sample correlation (dashed) in the (a) vertical and (b) horizontal for channel 6 of the AMSU-A radiances. The horizontal GGF and correlation are computed at the pressure level that has the maximal sample correlation.

temperature and wind speed than EnKF-GC for all lead times. Comparing Figure 10 with Figure 9, EnKF-FGGF has slightly smaller errors of temperature and wind speed than EnKF-GGF at all lead times, which is consistent with the verification against the ECWMF analyses from the 6 h priors and also the observation-space diagnostics.

4.4. Discussions

From the diagnostics in observation and model spaces, GGF outperforms GC, except that GGF has slightly larger errors than GC in the TR. *Lei et al*. [2015] conducted regional simulations and suggested that a deeper vertical localization was preferred for regions with precipitation than regions without precipitation, and similar results were obtained by *Montmerle and Berre* [2010] and *Caron and Fillion* [2010]. One possible explanation for GGF being slightly inferior to GC in the TR is that different vertical localization functions are needed for regions with and without active precipitation in the TR. Thus, the vertical GGF localization functions in the TR are computed for regions with and without precipitation separately based on the output of experiment EnKF-GC, although there is no cloudy radiance assimilated in the EnKF-GC. A surface grid point whose average precipitation rate in the past 3 h is larger than 0.00001 kg/(m^{2}s) is defined as a location with precipitation. For each channel, the horizontal GGF localization functions are also computed for regions with and without precipitation at the pressure level where the mean sample correlation maximizes [*Lei et al*., 2015].

Figure 11 shows the vertical and horizontal GGFs of channel 6 for regions with and without precipitation. The vertical GGF for regions with precipitation extends broader below 350 hPa than that for regions without precipitation. The horizontal GGF for regions with precipitation at pressure level 350 hPa has larger length scale than that for regions without precipitation. The mean sample correlations are consistent with the GGF. Thus regions with precipitation prefer broader localizations in both horizontal and vertical. Similar results are obtained for the other channels except channels 10–13 that are very high and have nearly no impact from precipitation. Although different localization functions may be preferred for regions with and without precipitation in the TR, an experiment that implements the localization functions varying with precipitating and nonprecipitating regions is not conducted here due to restrictions in the current GFS system configuration. Testing this hypothesis will be included in future work.

Another interesting point from the verifications in section 4.3 is that the FGGF is slightly better than the GGF. *Lei and Anderson* [2014a] showed that the GGF might overestimate the localization value when the estimated regression coefficients from the group of ensembles are not fully independent. Here it is possible that the GGF overestimates the localization value, especially when the correlation is closed to 0, since the group of ensemble perturbations is constructed from climatological ensemble perturbations. Moreover, as a GC localization function, the FGGF is smoother than the GGF, so the FGGF may have less sampling error projection onto the model's spurious numerical modes like gravity waves. Also other types of functions like

the spline used in *Lei and Anderson* [2014b] may be preferable for fitting the GGF; this will be explored in future work.

5. Conclusions

The concepts of vertical location and separation are not well defined for nonlocal observations like satellite radiances, so that localization for radiance observations is not straightforward. A global group filter (GGF) is adopted here to estimate the vertical localization for radiance observations. As an extension of the hierarchical ensemble filter proposed by *Anderson* [2007], the GGF does not require the observation locations and separations. It uses groups of estimated regression coefficients or correlations to provide an estimate of the localization function that minimizes the sampling error of the estimated properties from an ensemble assimilation system.

For idealized simulations where two kinds of background error covariances are designed, the GGF localization function is superior to the optimal GC localization function when assimilating a nonlocal observation. This result holds for varying ensemble sizes, although the error reduction of the GGF localization function relative to the optimal GC localization function decreases with increasing ensemble size. The GGF localization function has similar shape to the absolute value of the mean sample correlation. Unlike the optimal GC localization function, the GGF localization function can have local maxima when negative correlations are present.

The GGF is then used to offer a theoretical view of the vertical localization functions for the AMSU-A radiances. It automatically provides different vertical localization functions for each channel of the AMSU-A radiances, which also indicates the complexity and large computational cost to tune the localization scale for the radiance observations. Consistent with the results from the idealized simulation, the estimated vertical localization functions from the GGF have similar shapes to the absolute value of the mean sample correlations. When a prominent negative correlation occurs, a local maximum of the localization is obtained.

The GGF localization functions and fitted GGF localization functions (FGGF) are compared to the GC localization function using the NCEP GFS and the NOAA operational EnKF with assimilation of only the AMSU-A radiances. The 6 h priors from GC, GGF, and FGGF are verified relative to the conventional observations and the AMSU-A radiances, which show that the GGF and FGGF produce smaller errors than GC except in the tropics. Similar results are obtained when the 6 h priors are verified against the ECMWF analyses, and the advantages of the GGF and FGGF persist through 120 h forecast lead time.

It has been demonstrated that the GGF can provide appropriate vertical localization functions for the AMSU-A radiance observations and improve the assimilation of the AMSU-A radiances. Based on these encouraging results, the next step is to construct vertical localization functions for different state variables and various satellite platforms using the GGF, and then incorporate the estimated GGF vertical localization functions into the NCEP GFS and the NOAA operational EnKF. Moreover, adaptive algorithms that can provide localization functions along with assimilation but with affordable computational cost will be also explored.

Acknowledgement
This work was partially supported by the Disaster Relief Appropriations Act of 2013 (P.L. 113-2) that funded NOAA research grant NA14OAR4830123, the National Natural Science Foundation of China through Grants 41461164008 and 41130964. The data used to generate the simulation experiments were obtained from the National Centers for Environmental Prediction (NCEP). Thanks two anonymous reviewers whose valuable comments significantly improve the manuscript.

References

Aksoy, A., D. C. Dowell, and C. Snyder (2009), A multicase comparative assessment of the ensemble Kalman filter for assimilation of radar observations. Part I: Storm-scale analyses, *Mon. Weather Rev.*, *137*, 1805–1824.

Anderson, J. L. (2007), Exploring the need for localization in ensemble data assimilation using a hierarchical ensemble filter, *Physica D*, *230*, 99–111.

Anderson, J. L. (2009), Spatially and temporally varying adaptive covariance inflation for ensemble filters. *Tellus, Ser. A*, *61*, 72–83.

Anderson, J. L. (2012), Localization and sampling error correction in ensemble Kalman filter data assimilation, *Mon. Weather Rev.*, *140*, 2359–2371.

Anderson, J. L. (2016), Reducing correlation sampling error in ensemble Kalman filter data assimilation, *Mon. Weather Rev.*, *144*, 913–925.

Anderson, J. L., and S. L. Anderson (1999), A Monte Carlo implementation of the nonlinear filtering problem to produce ensemble assimilations and forecasts, *Mon. Weather Rev.*, *127*, 2741–2758.

Anderson, J. L., and L. Lei (2013), Empirical localization of observation impact in ensemble Kalman filters, *Mon. Weather Rev.*, *141*, 4140–4153.

Buehner, M., P. L. Houtekamer, C. Charette, H. L. Mitchell, and B. He (2010a), Intercomparison of variational data assimilation and the ensemble Kalman filter for global deterministic NWP. Part I: Description and single-observation experiments, *Mon. Weather Rev.*, *138*, 1550–1566.

Buehner, M., P. L. Houtekamer, C. Charette, H. L. Mitchell, and B. He (2010b), Intercomparison of variational data assimilation and the ensemble Kalman filter for global deterministic NWP. Part II: One-month experiments with real observations, *Mon. Weather Rev.*, *138*, 1567–1586.

Burgers, G., P. J. van Leeuwen, and G. Evensen (1998), Analysis scheme in the ensemble Kalman filter, *Mon. Weather Rev. 126*, 1719–1724.
Campbell, W. F., C. H. Bishop, and D. Hodyss (2010), Vertical covariance localization for satellite radiances in ensemble Kalman filters, *Mon. Weather Rev.*, *138*, 282–290.
Caron, J.-F., and L. Fillion (2010), An examination of background error correlations between mass and rotational wind over precipitation regions, *Mon. Weather Rev.*, *138*, 563–578.
Collard, A. D., and A. P. McNally (2009), The assimilation of infrared atmospheric sounding interferometer radiances at ECMWF, *Q. J. R. Meteorol. Soc.*, *135*, 1044–1058.
Derber, J. C., and W.-S. Wu (1998), The use of TOVS cloud-cleared radiances in the NCEP SSI analysis system, *Mon. Weather Rev.*, *126*, 2287–2299.
Evensen, G. (1994), Sequential data assimilation with a nonlinear quasi-geostrophic model using Monte Carlo methods to forecast error statistics, *J. Geophys. Res.*, *99*(C5), 10,143-10,162.
Fertig, E. J., B. R. Hunt, E. Ott, and I. Szunyogh (2007), Assimilating non-local observations with a local ensemble Kalman filter, *Tellus, Ser. A*, *59*, 719–730.
Gaspari, G., and S. E. Cohn (1999), Construction of correlation functions in two and three dimensions, *Q. J. R. Meteorol. Soc.*, *125*, 723–757.
Hamill, T. M., J. S. Whitaker, and C. Snyder (2001), Distance-dependent filtering of background-error covariance estimates in an ensemble Kalman filter, *Mon. Weather Rev.*, *129*, 2776–2790.
Hamurd, M., M. Bonavita, and L. Isaksen (2015), EnKF and hybrid gain ensemble Kalman filter data assimilation. Part I: EnKF implementation, *Mon. Weather Rev.*, *143*, 4847–4864.
Han, Y., F. Weng, Q. Liu, and P. van Delst (2007), A fast radiative transfer model for SSMIS upper atmosphere sounding channels, *J. Geophys. Res.*, *112*, D11121, doi:10.1029/2006JD008208.
Houtekamer, P. L., and H. L. Mitchell (2001), A sequential ensemble Kalman filter for atmospheric data assimilation, *Mon. Weather Rev.*, *129*, 123–137.
Houtekamer, P. L., and H. L. Mitchell (2005), Ensemble Kalman filtering, *Q. J. R. Meteorol. Soc.*, *131*, 3269–3289.
Houtekamer, P. L., H. L. Mitchell, G. Pellerin, M. Buehner, M. Charron, L. Spacek, and B. Hansen (2005), Atmospheric data assimilation with the ensemble Kalman filter: Results with real observations, *Mon. Weather Rev.*, *133*, 604–620.
Houtekamer, P. L., X. Deng, H. L. Mitchell, S. Baek, and N. Gagnon (2014), Higher resolution in an operational ensemble Kalman filter, *Mon. Weather Rev.*, *142*, 1143–1162.
Kalman, R. E. (1960), A new approach to linear filtering and prediction problems, *J. Basic Eng.*, *82D*, 35–45.
Kleist, D. T., D. F. Parrish, J. C. Derber, R. Treadon, W. Wu, and S. Lord (2009), Introduction of the GSI into NCEP Global Data Assimilation System, *Weather Forecasting*, *24*, 1691–1705.
Lei, L., and J. L. Anderson (2014a), Comparisons of empirical localization techniques for serial ensemble Kalman filters in a simple atmospheric general circulation model, *Mon. Weather Rev.*, *142*, 739–754.
Lei, L., and J. L. Anderson (2014b), Empirical localization of observations for serial ensemble Kalman filter data assimilation in an Atmospheric General Circulation Model, *Mon. Weather Rev.*, *142*, 1835–1851.
Lei, L., and J. S. Whitaker (2015), Model space localization is not always better than observation space localization for assimilation of satellite radiances, *Mon. Weather Rev.*, *143*(10), 3948–3955.
Lei, L., J. L. Anderson, and G. S. Romine (2015), Empirical localization functions for ensemble Kalman filter data assimilation in regions with and without precipitation, *Mon. Weather Rev.*, *143*, 3664–3679.
Le Marshall, J., et al. (2006), Improving global analysis and forecasting with AIRS, *Bull. Am. Meteorol. Soc.*, *87*, 891–894.
McCarty, W., G. Jedlovec, and T. L. Miller (2009), Impact of the assimilation of Atmospheric Infrared Sounder radiance measurements on short-term weather forecasts, *J. Geophys. Res.*, *114*, D18122, doi:10.1029/2008JD011626.
McNally, A. P., P. D. Watts, J. A. Smith, R. Engelen, G. A. Kelly, J. N. Thepaut, and M. Matricardi (2006), The assimilation of AIRS radiance data at ECMWF, *Q. J. R. Meteorol. Soc.*, *132*, 935–957.
Miyoshi, T., and Y. Sato (2007), Assimilating satellite radiances with a local ensemble transform Kalman filter (LETKF) applied to the JMA global model (GSM), *SOLA*, *3*, 37–40.
Miyoshi, T., Y. Sato, and T. Kadowaki (2010), Ensemble Kalman filter and 4D-Var intercomparison with the Japanese Operational Global Analysis and Prediction System, *Mon. Weather Rev.*, *138*, 2846–2866.
Montmerle, T., and L. Berre (2010), Diagnosis and formulation of heterogeneous background-error covariances at the mesoscale, *Q. J. R. Meteorol. Soc.*, *136*, 1408–1420.
Ota, Y., J. C. Debber, E. Kalnay, and T. Miyoshi (2013), Ensemble-based observation impact estimates using the NCEP GFS, *Tellus Ser. A*, *65*, 20038.
Otkin, J. A. (2012), Assessing the impact of the covariance localization radius when assimilating infrared brightness temperature observations using an ensemble Kalman filter, *Mon. Weather Rev.*, *140*, 543–561.
Palmer, T. N., R. Buizza, F. Doblas-Reyes, T. Jung, M. Leutbecher, G. J. Shutts, M. Steinheimer, and A. Weisheimer (2009), Stochastic parameterization and model uncertainty, *ECMWF Tech. Memo. 598*, 44 pp., Eur. Cent. for Medium-Range Weather Forecasts, Reading, U. K. [Available at http://www.ecmwf.int/sites/default/files/elibrary/2009/11577-stochastic-parametrization-and-model-uncertainty.pdf.]
Snyder, C., and F. Zhang (2003), Assimilation of simulated Doppler radar observations with an ensemble Kalman filter, *Mon. Weather Rev.*, *131*, 1663–1677.
Tong, M., and M. Xue (2005), Ensemble Kalman filter assimilation of Doppler radar data with a compressible nonhydrostatic model: OSS experiments, *Mon. Weather Rev.*, *133*, 1789–1807.
Weng, F. (2007), Advances in radiative transfer modeling in support of satellite data assimilation, *J. Atmos. Sci.*, *64*, 3799–3807.
Whitaker, J. S., and T. M. Hamill (2002), Ensemble data assimilation without perturbed observations, *Mon. Weather Rev.*, *130*, 1913–1924.
Whitaker, J. S., and T. M. Hamill (2012), Evaluating methods to account for system errors in ensemble data assimilation, *Mon. Weather Rev.*, *140*, 3078–3089.
Whitaker, J. S., T. M. Hamill, X. Wei, Y. Song, and Z. Toth (2008), Ensemble data assimilation with the NCEP Global Forecast System, *Mon. Weather Rev.*, *136*, 463–482.
Wu, W. S., R. J. Purser, and D. F. Parrish (2002), Three-dimensional variational analysis with spatially inhomogeneous covariances, *Mon. Weather Rev.*, *130*, 2905–2916.
Zapotocny, T. H., J. A. Jung, J. F. Le Marshall, and R. E. Treadon (2008), A two-season impact study of four satellite data types and rawinsonde data in the NCEP Global Data Assimilation System, *Weather Forecasting*, *23*, 80–100.